Spatial structure in Neptune's 7.90-μm stratospheric CH_4 emission, as measured by VLT-VISIR

J. A. Sinclair[a,], G. S. Orton[a], L. N. Fletcher[b], M. Roman[b], I. de Pater[c], T. Encrenaz[d], H. B. Hammel[e], R. S. Giles[a,f], T. Velusamy[a], J. I. Moses[g], P. G. J. Irwin[h], T. W. Momary[a], N. Rowe-Gurney[b], F. Tabataba-Vakili[a]

[a] *Jet Propulsion Laboratory/California Institute of Technology, 4800 Oak Grove Dr, Pasadena, CA 91109, United States*

[b] *School of Physics & Astronomy, University of Leicester, University Road, Leicester, LE1 7RH, United Kingdom*

[c] *University of California at Berkeley, 501 Campbell Hall #3411, Berkeley, CA 94720, United States*

[d] *L'Observatoire de Paris, Observatoire Paris-Site de Meudon, LESIA, 5 Pl Jules Janssen, 92195 Meudon Cedex, France*

[e] *Association of Universities for Research in Astronomy, 1331 Pennsylvania Avenue NW - Suite 1475, Washington, DC 20004, United States*

[f] *Southwest Research Institute, 6220 Culebra Road, San Antonio, TX 78238, United States*

[g] *Space Science Institute, 4750 Walnut St, Suite 205, Boulder, CO 80301, United States*

[h] *Atmospheric, Oceanic & Planetary Physics, University of Oxford, Parks Road, Oxford, OX1 3PU, United Kingdom*

Abstract

We present a comparison of VLT-VISIR images and Keck-NIRC2 images of Neptune, which highlight the coupling between its troposphere and stratosphere. VLT-VISIR images were obtained on September 16th 2008 (UT) at 7.90 μm and 12.27 μm, which are primarily sensitive to 1-mbar CH_4 and C_2H_6 emission, respectively. NIRC2 images in the H band were obtained on

Email address: james.sinclair@jpl.nasa.gov (J. A. Sinclair)

October 5th, 6th and 9th 2008 (UT) and sense clouds and haze in the upper troposphere and lower stratosphere (from approximately 600 to 20 mbar). At 7.90 μm, we observe enhancements of CH_4 emission in latitude bands centered at approximately 25°S and 48°S (planetocentric). Within these zonal bands, tentative detections ($< 2\sigma$) of discrete hotspots of CH_4 emission are also evident at 24°S, 181°W and 42°S, 170°W. The longitudinal-mean enhancements in the CH_4 emission are also latitudinally-coincident with bands of bright (presumably CH_4 ice) clouds in the upper troposphere and lower stratosphere evidenced in the H-band images. This suggests the Neptunian troposphere and stratosphere are coupled in these specific regions. This could be in the form of 1) 'overshoot' of strong, upwelling plumes and advection of CH_4 ice into the lower stratosphere, which subsequently sublimates into CH_4 gas and/or 2) generation of waves by plumes impinging from the tropopause below, which impart their energy and heat the lower stratosphere. We favor the former process since there is no evidence of similar smaller-scale morphology in the C_2H_6 emission, which probes a similar atmospheric level. However, we cannot exclude temperature variations as the source of the morphology observed in CH_4 emission. Future, near-infrared imaging of Neptune performed near-simultaneously with future mid-infrared spectral observations of Neptune by the James Webb Space Telescope would allow the coupling of Neptune's troposphere and stratosphere to be confirmed and studied in greater detail.

Keywords:

---

1. Introduction

Neptune's troposphere is highly dynamic. Previous ultraviolet to near-infrared measurements of Neptune have demonstrated a wealth of variable phenomena in its upper troposphere. These include a series of dark oval features, the largest of which is denoted 'the Great Dark Spot' (Hammel et al., 1995; Smith et al., 1989; Sromovsky et al., 2001; Wong et al., 2018), latitudinal banding related to the distributions of haze and methane humidity (Karkoschka and Tomasko, 2011; Karkoschka, 2011) and cloud phenemona (Roddier et al., 1998, 2000; Max et al., 2003; Gibbard et al., 2002, 2003; Irwin et al., 2011) with variability on daily to annual timescales (Sromovsky et al., 1995, 2001; Lockwood and Jerzykiewicz, 2006; Hammel and Lockwood, 2007; Luszcz-Cook et al., 2010).

The extent to which Neptune's stratosphere is dynamic and/or coupled to the troposphere is less certain. Neptune's stratosphere is sensed through the mid-infrared emission features of CH_4 and its photochemical products: C_2H_2, C_2H_4 and C_2H_6 (e.g. Gillett and Rieke 1977; Orton et al. 1987, 1992; Schulz et al. 1999; Fletcher et al. 2010; Greathouse et al. 2011; Fletcher et al. 2014). At such wavelengths, the effects of seeing and particularly diffraction, combined with Neptune's cooler temperatures and small angular size from Earth, make resolving spatial features a challenge. In general, the lack of spectral sensitivity and spatial resolution in earlier studies only allowed the stratosphere of Neptune to be studied in a disk-integrated or zonal-mean sense (e.g. Conrath et al. 1989, 1991; Bezard et al. 1991; Bézard et al. 1999; Schulz et al. 1999; Fouchet et al. 2003; Meadows et al. 2008;

Lellouch et al. 2015). Nevertheless, such studies revealed a surprising result: the stratospheric partial pressure of CH_4 on Neptune (Lellouch et al., 2010, 2015) is larger than its saturation vapor pressure at the tropopause (Baines and Hammel, 1994; Sánchez-Lavega et al., 2004). This implies gaseous CH_4 is being delivered into the lower stratosphere, above altitudes where it would be expected to condense into CH_4 ice, as discussed in Stoker et al. (1987) and Lunine and Hunten (1989).

Only once mid-infrared spectroscopy or imaging was performed on diffraction-limited 8-m- or larger-class telescopes could the spatial structure of Neptune's stratosphere be studied. Keck-LWS (Long Wave Spectrometer, Jones and Puetter 1993) spatially-resolved spectroscopic observations in 2003 first revealed the presence of enhanced CH_4 and C_2H_6 emission in its south polar region (de Pater et al., 2014). This was later confirmed by Gemini-MICHELLE (Mid-Infrared Echelle Spectrograph, Glasse et al. 1997) measurements in 2005 (Hammel et al., 2007). VLT-VISIR (Very Large Telescope Spectrometer and Imager for the Mid-Infrared, Lagage et al. 2004) images of Neptune measured in 2006 similarly revealed the presence of a warm, south polar stratosphere and also demonstrated the troposphere was bright in mid-infrared emission (Orton et al., 2007; Encrenaz et al., 2007). The bright south-polar stratospheric emission was absent from Voyager measurements recorded in 1989 (Fletcher et al., 2014), as well as Gemini-North-TEXES (Texas Echelon Cross Echelle Spectrograph, Lacy et al. 2002) spectra measured in 2007 (Greathouse et al., 2011). This could suggest the southern polar hotspot is a transient phenomenon and/or it is offset from the pole and happened to be on the opposing hemisphere at the time of these measurements. However, it is more likely that the bright,

south polar hotspot was not resolved by the TEXES observations due to their adopted method of scan mapping Neptune. The geometry chosen for the scan mapping resulted in only a 0.5" spatial resolution along Neptune's central meridian, which is a significant fraction of Neptune's disk and much larger than the FWHM of the south polar hot spot. The southern polar hotspots were first suggested to result from a planetary wave propagating from the troposphere to the stratosphere (e.g. Orton et al. 2012). The warmer, tropospheric temperatures were interpreted to allow gaseous CH_4, normally cold-trapped below the ∼200-mbar level, to 'leak' up into the lower stratosphere, thereby further enhancing its mid-infrared emission. In contrast, Fletcher et al. (2014) and de Pater et al. (2014) suggested the southern polar hotspots were due to adiabatic heating from subsiding air in a polar vortex.

Fletcher et al. (2014) characterized longitudinal-mean properties of Neptune's atmosphere near southern summer solstice from mid-infrared images acquired at several different telescopes and, de Pater et al. (2014) deduced the global circulation on Neptune from a comparison of Neptune images at mid-infrared, near-infrared and radio wavelengths. Mid-southern latitudes were observed to be dimmer at mid-infrared wavelengths, and near-infrared images highlighted the prevalence of both spatially-extended and -intermittent clouds between the 600- and 20-mbar levels. This was interpreted as rising air at mid-southern latitudes as part of a larger-scale circulation, with the associated adiabatic cooling resulting in dimmer mid-infrared emission and clouds resulting from the condensation of CH_4. The authors suggest that the stratospheric clouds may be the tops of anticyclones and that these clouds are connected from

the troposphere through the tropopause into the stratosphere.

In this work, we present images of Neptune measured by VLT-VISIR in September 2008 at 7.9 and 12.27 μm (Section 2.1), which respectively capture stratospheric CH_4 and C_2H_6 emission. These are a subset of images published by Orton et al. (2012). In particular, the 7.90-μm image was measured during relatively stable atmospheric conditions and thus the best seeing-limited spatial resolution. The high spatial resolution, which we attempt to augment with image deconvolution, has allowed spatial structure in the stratospheric CH_4 emission to be resolved near the sub-observer point at mid-southern latitudes. We compare these mid-infrared images with those measured in the H-band (1.633 μm) several weeks later (Section 2.2) in order to compare the spatial structure in the stratospheric emission with the morphology of clouds.

2. Observations

2.1. VLT-VISIR

Mid-infrared images of Neptune were measured using the VISIR (VLT Spectrometer and Imager for the Mid-Infrared, Lagage et al. 2004) instrument on the 8.2-m Melipal telescope at the European Southern Observatory's Very Large Telescope. Images were recorded on September 16th 2008 (UTC). We focus this study on the images measured in the 7.90- and 12.27-μm filters, which respectively capture Neptune's stratospheric CH_4 and C_2H_6 emission predominantly from the 10- to 0.1-mbar pressure range (Figure B.1).

VISIR's 256 x 256 pixel array and pixel scale of 0.075" resulted in a total

field-of-view of approximately 19 x 19" covering Neptune's 2.34" diameter disk and background sky. Chopping and nodding were performed in order to remove sky background emission. For radiometric calibration and measurement of the point-spread function (PSF) for image deconvolution, similar images were also measured of HD 216032 (tau Aqr), which is an M0III star with absolutely-calibrated mid-infrared radiances (Cohen et al., 1999). Further details of the VISIR images measured of Neptune and HD 216032 are provided in Table A.1 of the Appendix.

2.1.1. Image reduction & calibration

The initial reduction, including the A-B subtraction and flatfielding, was performed using instrument-specific software provided by ESO for the VLT. Despiking and bad-pixel removal were performed using techniques described in greater detail in Fletcher et al. (2009). Individual images of Neptune were then aligned and coadded in order to increase the signal-to-noise ratio. A Fourier filter was applied to remove high frequency noise. The resulting images are shown in Figure 1 a, b.

A limb-fitting procedure was used to assign latitudes, longitudes and emission angles to the images of Neptune, which were then projected cylindrically. In each latitude band, a quadratic polynomial fit was performed of the radiance vs. $\mu = \cos(\theta_{\rm emm})$ distribution (where $\theta_{\rm emm}$ is the emission angle) in order to correct for the foreshortening and centre-to-limb brightening in the longitudinal direction. We chose not to perform the correction in the latitudinal correction in case physical, meridional variations in emission were removed. Using published fluxes of HD 216032 between 8.0 and 24.5 μm

in discrete filters (Cohen et al., 1999), the flux values in the 7.90- and 12.27-μm VISIR filters were estimated by linear interpolation. Circular photometry was performed on the images of HD 216032 to calculate the total counts measured from the star, with respect to the background. Radiometric calibration scale factors were derived in order to convert the images of Neptune into units of spectral radiance (also taking into account differences in the total exposure time and airmass). Figures 1 c and d show the cylindrically-projected and absolutely-calibrated images in brightness temperature units. We find that the ranges in brightness temperature of the calibrated images are consistent with previous studies of Neptune at similar wavelengths and epochs (Orton et al., 2007; Encrenaz et al., 2007; Fletcher et al., 2014; de Pater et al., 2014). The noise-equivalent spectral radiance (NESR) of the images were calculated by finding the standard deviation of sky pixels in the calibrated images of Neptune. We derived NESR values of 21.77 and 41.31 pW cm^{-2} sr^{-1} $(cm^{-1})^{-1}$ at 7.90 and 12.27 μm, respectively. These correspond to noise-equivalent brightness temperatures of 0.48 K at 115 K at 7.90 μm and 0.20 K at 90 K at 12.27 μm.

2.1.2. Deconvolution

We attempted to perform a deconvolution of the images in order to augment and sharpen spatial details. At each wavelength, the image of HD 216032 was adopted as the point-spread function (PSF) and a Richardson-Lucy Maximum Correlation Method (RLMCM) deconvolution (Richardson, 1972; Lucy, 1974) was performed in an attempt to remove the effects of atmospheric seeing and diffraction. The deconvolved image was then projected cylindrically

and a centre-to-limb correction (as detailed in Section 2.1.1) was applied. Figure 2 shows the 7.90-μm image of Neptune after 30 iterations of the RLMCM deconvolution. The deconvolution appears to have been successful with spatial structure near the sub-observer point becoming more prominent. In order to account for the amplification of random noise by the deconvolution, we re-calculated the NESR by finding the standard deviation of all sky pixels. We derived a value of 37.7 pW cm^{-2} sr^{-1} $(cm^{-1})^{-1}$, which is a factor of 1.7 higher than the value derived from Figure 1 before deconvolution. This corresponds to a noise-equivalent brightness temperature of 0.82 K at 115 K.

In contrast, the deconvolution of the 12.27-μm image was problematic and did not produce a physically-sensible image. We note that the images of Neptune and HD216032 at 7.90 μm were measured less than two hours apart, at similar airmasses and seeing conditions (Table A.1). In contrast, the images of HD 216032 and Neptune at 12.27 μm were measured more than 3 hours apart, at different airmasses and during different seeing conditions. This is likely why the deconvolution at 12.27 μm was less successful compared to 7.90 μm. We also attempted to perform the deconvolution at 12.27 μm using a theoretical airy disk as the PSF, although this was similarly unsuccessful. We have therefore omitted the deconvolved 12.27-μm image from the results and henceforth refer to the 12.27-μm image shown in Figure 1d (before deconvolution).

2.1.3. Longitudinal-mean emission

In order to determine overall meridional variations, we calculated the mean emission over all sampled longitudes in the 7.90 μm and 12.27 μm images (using the images corrected for centre-to-limb variation). For 7.90 μm, this calculation was also performed for the image after deconvolution was performed. We will henceforth describe this as a 'longitudinal mean' for simplicity though we remind the reader that results derived only capture a subset of longitudes and not a true longitudinal or zonal mean (of 0 - 360° in longitude). The error on the longitudinal mean was calculated in two ways. Firstly, the standard deviation on the mean was calculated in order to capture the longitudinal variability of emission in each latitude band. Secondly, the aforementioned NESR values were scaled by a factor of $n_{pixels}^{-0.5}$, where n_{pixels} is the number of pixels on the disk of Neptune in each latitude band. The mean emission ($\bar{R}$) was then converted into brightness temperature (T_B) and the errors calculated by T_B ($\bar{R} + \sigma$) - T_B. The standard deviation on the mean (capturing longitudinal variability) was found to be the larger of the two errors and is henceforth quoted as the 1-σ error, unless otherwise stated.

2.2. Keck-NIRC2 imaging

H-band images of Neptune were measured on October 5-9th 2008 UT using NIRC2 (Near Infrared Camera 2, Wizinowich et al. 2000) coupled to the adaptive optics system at the Keck II telescope. NIRC2 has a 1024 x 1024 Aladdin InSb detector, which was used in its high-angular-resolution 'narrow' mode resulting in a pixel scale of 9.94 ± 0.03 milliarcseconds (mas) (de Pater

et al., 2006, 2014). We selected three images, based on their quality and their central-meridian longitudes, which collectively provided nearly 360° in longitudinal coverage. Further details of each image are provided in Table A.2 of the Appendix.

Since we are only interested in the morphology of the cloud coverage, we did not photometrically calibrate the images, but merely normalized them to the brightest on-planet pixel in each image. We reduced images using standard infrared data reduction techniques of sky subtraction, flat-fielding and median-value masking to remove hot and cold pixels. A 3-σ gaussian filter was performed to remove corrupted pixels and a Fourier filter was applied to remove high-frequency noise. The resulting noise on the normalized image was then estimated by finding the standard deviation of all background, sky pixels. A limb-fitting procedure was subsequently used to assign geometry to the images (as described previously in Section 2.1.1) and the images were projected cylindrically. Figure 3 shows the original and cylindrically-projected NIRC2 images of Neptune. The images are not absolutely calibrated and thus simply show the normalized reflectivity of Neptune resulting from clouds and haze in its upper troposphere and lower stratosphere. Using a similar calculation as detailed further in Section 2.1.3, the longitudinal-mean (normalized) H-band reflectivity was also calculated as a function of latitude.

3. Results & Discussion

Neptune's south pole is bright in both CH_4 and C_2H_6 emission as in previous work (e.g. Encrenaz et al. 2007; Hammel et al. 2007; Orton et al. 2007; Fletcher et al. 2014; de Pater et al. 2014). From the equator to 85°S,

the longitudinal-mean brightness-temperature exhibits a net increase from 114.9 ± 0.1 K to 118.4 ± 0.3 K in 7.90-μm CH_4 emission and from 89.9 ± 0.2 K to 92.6 ± 0.38 K in 12.27-μm C_2H_6 emission (using values from the centre-to-limb corrected images before deconvolution). Orton et al. (2007, 2012) attributed the southern-polar hotspot to a disturbance propagating upwards from the troposphere to the stratosphere, manifesting as a low-wavenumber wave feature, which would enhance the brightness temperature in the CH_4 and C_2H_6 emission features. Warm tropospheric temperatures at the south pole would also significantly weaken the cold trap and allow methane gas to diffuse more freely through the tropopause to the lower stratosphere, which would further augment the enhanced CH_4 emission. However, Fletcher et al. (2014) attributed the southern-polar hotspot to adiabatic heating by subsiding air as part of larger-scale meridional circulation and/or a polar cyclonic vortex, similar to the summer polar vortices observed on Saturn (Fletcher et al., 2008; Sinclair et al., 2013; Fletcher et al., 2015; Fletcher et al., 2018). de Pater et al. (2014) also found Neptune's south pole to be bright at radio wavelengths, which demonstrates the air as deep as the ∼40-bar level is low in humidity, which is also consistent with subsiding air dessicated from higher altitudes in contrast to an upward propagation.

From the equator to mid-northern latitudes, the larger-scale emission at both 7.90 and 12.27 μm increases. Dimmer and brighter spots of CH_4 emission ($\Delta T_B \sim 0.4$ K) are apparent at mid-northern latitudes though are not significant with respect to uncertainty (∼0.8 K). From 10-70°S, the larger-scale emission at 7.90 μm and 12.27 μm (Figure 1, 2) appears colder compared to north of the equator and the south pole. This is in agreement

with infrared measurements made by Voyager (Conrath et al., 1989) as well as in mid-infrared images obtained between 2003 and 2007 (de Pater et al., 2014; Fletcher et al., 2014). This has been attributed to a global circulation system with upwelling air and the associated adiabatic cooling at mid latitudes and dry, descending air over the poles and equator (Bezard et al., 1991; Conrath et al., 1991; de Pater et al., 2014).

The images of Neptune at 7.90 and 12.27 μm are shown again in Figure 4 but focusing on low-to-high southern latitudes and with a color scale that enhances smaller-scale morphology. The 12.27-μm image of C_2H_6 emission is relatively featureless in smaller-scale morphology whereas the 7.90-μm image shows bands of enhanced CH_4 emission extended in longitude at latitudes of approximately 48°S and 25°S. This is further demonstrated in Figure 5, which shows the longitudinal-mean emission at 7.90 and 12.27 μm as a function of latitude. From 25°S to 37°S, the longitudinal-mean 7.90-μm emission decreases from 111.85 ± 0.07 K to 113.38 ± 0.06 K in brightness temperature (quoting brightness temperatures and noise values derived from the 7.90-μm image before deconvolution). Similarly, from 37°S to 46°S, the longitudinal-mean 7.90-μm emission increases from 111.85 ± 0.07 K to 112.93 ± 0.06 K.

Discrete hotspots of enhanced emission near-coincident within the brighter latitudes are also apparent in Figures 2 and 4. The most prominent hotspots appear at 24°S, 182°W and 45°S, 170°W and also appear evident even before image deconvolution was performed (Figure 1c). Adopting the brightness temperature and sensitivity values from Figure 2 after image deconvolution, the hotspots are respectively $\Delta T_B = 1.9 \pm 1.1$ K and 2.0 ± 1.1 K higher in

brightness temperature compared to surrounding regions in the same latitude band. These enhancements are not significant with respect to the 2-σ level and thus are considered tentative detections. We thus focus our discussion on longitudinal-mean variations in mid-infrared emission rather than individual features.

Using a radiative-transfer forward model, we computed 7.90-μm brightness temperatures for a range of vertical profiles of temperature and CH_4 (see Appendix B for further details). As shown in Figure B.2, an observed, ∼2 K variation in the 7.90-μm brightness temperature would require either a ∼5-K variation in atmospheric temperature centered at the 0.8-mbar level or an enrichment in the 0.8-mbar CH_4 abundance by a factor of 2. Changes in the CH_4 abundance have no effect on the 12.27-μm emission however, a ∼5-K atmospheric temperature variation centered at the 0.8-mbar level would produce at least a 1.5-K change in brightness temperature at 12.27 μm. This is significant with respect to the estimated noise-equivalent brightness temperature (0.2 K) and thus should be detectable in the observed image at 12.27 μm. However, we do not find evidence of similar enhancements (either discrete or overall in latitude) in the image at 12.27 μm of C_2H_6 emission (Figure 1), which sounds a similar level of the atmosphere (Figure B.1). As discussed in greater detail below, this is suggestive that CH_4 gas variations are the source of the observed morphology though we cannot completely rule out a temperature origin.

In the H-band, mid-southern latitudes are host to both spatially extended and intermittent cloud features (e.g. de Pater et al. 2014; Irwin et al. 2016). Similar though significantly foreshortened cloud features are also

present at mid-to-high northern latitudes. de Pater et al. (2014) performed a spectral analysis of Keck-NIRC2 images obtained in October 2003 between 1.25 and 2.27 μm and were able to constrain the clouds into two layers: a deeper (300 to 600 mbar) layer of spatially-extended clouds as well as spatially-intermittent clouds at lower pressures of 20 - 30 mbar, both likely made of CH_4 ice, which would be expected to evaporate at pressures lower than 20 mbar (Sánchez-Lavega et al., 2004). The latter, lower stratospheric clouds were interpreted as resulting from strong, localized upwelling events.

We explored the possibility of a link between the tentative mid-infrared hotspots and the discrete cloud features at near-infrared wavelengths. Using the zonal-wind speeds derived by Tollefson et al. (2018) from H-band images of Neptune, we extrapolated the longitudinal position of the 7.90-μm hotspots to the time of measurement of the near-infrared images (20, 23 and 24 days later). We found no obvious *longitudinal* correlation between the mid-infrared and near-infrared, however, in hindsight, this was unsurprising. Firstly, we note the standard deviation in zonal-wind speeds derived by Tollefson et al. (2018) increases from ∼50 m/s at 25°S to ∼ 100 m/s at 45°S. In either case, this corresponds to an uncertainty in longitude of much greater than 360° after a period of 19-23 days (which is the time elapsed between the mid-infrared and near-infrared images). Secondly, a parcel of air will experience a different zonal-wind speed as it rises to lower pressures and thus, a single zonal-wind speed would introduce errors into a calculation of its longitudinal propagation. Thirdly, cloud features on Neptune have been observed to form, evolve and dissipate rapidly, even on timescales as short as minutes (e.g. Limaye and Sromovsky 1991; Sromovsky et al. 1993, 2001;

Martin et al. 2012) and thus the individual clouds present at the time of the NIRC2 measurements may not have been present at the time of the VISIR measurements.

Nevertheless, the *latitudinal* coincidence of brighter mid-infrared emission at 7.90μm and near-infrared cloud features is suggestive of a link. Figure 5 compares the longitudinal-mean brightness temperature at 7.90 μm with the longitudinal-mean H-band reflectivity. As shown, both the mid-infrared 7.90-μm CH_4 emission and H-band reflectivity peak at similar latitudes of 25-30°S and 50°S. We suggest two reasons for the source of this link.

Firstly, strong, tropospheric upwelling in the troposphere could 'overshoot' the tropopause and reach the lower stratosphere. CH_4 ice advected in the upwelling region could sublimate at pressures lower than approximately 20 mbar (Sánchez-Lavega et al., 2004). Assuming the plume continues rising in altitude to pressures lower than 10 mbar, where CH_4 ice is expected to sublimate (Sánchez-Lavega et al., 2004), this would enhance the CH_4 gaseous abundance and thus 7.90-μm CH_4 emission, which is sensitive to the 10- to 0.1-mbar level (Figure B.1). While C_2H_6 is a photochemical product of CH_4, C_2H_6 cannot be efficiently photochemically produced in the lower stratosphere and thus this process would only enrich the lower stratospheric CH_4. While tropospheric, gaseous CH_4 is depleted by a factor of ∼2 at mid-to-high southern latitudes compared to elsewhere on the planet (e.g. Karkoschka and Tomasko 2011; Luszcz-Cook et al. 2016; Irwin et al. 2019), the resulting partial pressure of tropospheric CH_4 is still higher than its stratospheric counterpart. Thus, in addition to the CH_4 in solid phase that eventually sublimates, we believe there is a sufficient reservoir of CH_4 below

the tropopause such that an upwelling plume would enrich the abundance of CH_4 at stratospheric altitudes. An upwelling plume of CH_4 ice, and eventually CH_4 gas, would be advected and diffused in longitude and latitude. According to Figure 7 of Moses et al. (2018), the diffusion timescale at 1 mbar is approximately 20 Earth years. However, using temperature maps retrieved from Keck-LWS measurements and the thermal wind equation, Fletcher et al. (2014) derived zonal-wind speeds of $\sim$190 m/s and $\sim$100 m/s at 25°S and 45°S, respectively. Thus, over a 24-hour period, a parcel of air would travel approximately 265° and 180° in longitude at 25°S and 45°S, respectively. Thus, plumes of upwelling CH_4 gas would likely be zonally advected over significantly shorter timescales than meridional advection or diffusion. In addition, zonal wind shear in the meridional direction would smear out a discrete plume to a larger range in longitude, which would create the observed latitudinal bands of enhanced CH_4 emission at 7.90 μm. If the tentative hotspots of CH_4 emission within these enhanced latitudinal bands are interpreted at face value, their presence implies they are the result of very recent ($<$ several days) injections.

Secondly, the strong, tropospheric upwelling could impart energy and mechanically force the lower stratosphere. For example, the northern mid-latitude storm on Saturn of late 2010, which produced significant temperature enhancements of up to 80 K in the stratospheric 'beacon', was believed to have been triggered initially by a tropospheric disturbance, which subsequently imparted energy into the stratosphere through the generation of waves (Fletcher et al., 2011, 2012; Sánchez-Lavega et al., 2012). A similar mechanism could produce temperature enhancements in the lower stratosphere of Neptune, thereby

enhancing both the 7.90-μm CH_4 emission and 12.27-μm C_2H_6 emission. The observed 2 K variation in 7.90-μm brightness temperature could result from variations in stratospheric temperature at 0.8 mbar of approximately 5 K - see Appendix B. By the thermal wind equation, latitudinal bands of enhanced temperature would signify the presence of zonal wind shears at the 1-mbar level compared to adjacent latitude bands. However, if the banding of 7.90-μm emission is indeed due to enhanced stratospheric temperatures, a similar morphology would also be expected of the C_2H_6 emission at 12.27 μm. This is because both the 7.90-μm CH_4 and 12.27-μm C_2H_6 emission sound the 1-mbar level (Figure B.1) according to the model atmosphere assumed in our radiative transfer model (see Appendix B). Indeed, forward models demonstrate that the 5-K atmospheric temperature variation, which is needed to produce the observed 2-K brightness temperature increase at 7.90 μm, would also produce a 1.5 - 2 K brightness temperature variation at 12.27 μm. This variation would be measurable with respect to the estimated 0.2 K noise-equivalent brightness temperature at 12.27 μm (Section 2.1.1). Yet, similar enhancements of C_2H_6 emission at 24°S and 48°S are not observed. Although the diffraction-limited spatial resolution decreases with wavelength, Figure 6a demonstrates that the morphology observed at 7.90 μm should still be resolved with the 12.27-μm PSF. Thus, the fact that the 12.27-μm image is absent of any banding is suggestive the morphology observed of the 7.90-μm CH_4 emission is due to CH_4 gas variations. However, we do not completely exclude temperature variations as a possibility.

Future mid-infrared and near-infrared measurements would provide the means to confirm these banding features and (tentative) hotspots and distinguish

between the hypothesized processes that produce them. Near-simultaneous measurements at near-infrared and mid-infrared wavelengths would provide a more conclusive connection between upwelling plumes evidenced in the H-band and their forcing of the lower stratosphere sensed at mid-infrared wavelengths. VLT-VISIR imaging of Neptune at 7.90 and 12.27 μm with measurements of a nearby star to characterize the PSF as close as possible in time, would optimize the deconvolution and enable any smaller-scale morphology in the C_2H_6 and CH_4 emission to be observed and compared. MIRI (Mid-Infrared Instrument, Rieke et al. 2015) onboard JWST (the James Webb Space Telescope) will allow spectroscopy of Neptune in the 5- to 30-μm range to be performed at a very high sensitivity (Norwood et al., 2016). The coarser pixel scale (0.196–0.273") and diffraction-limited spatial resolution (∼0.3") of JWST-MIRI (James Webb Space Telescope's Mid-Infrared Instrument, Rieke et al. 2015) would not be able to resolve discrete hotspots in stratospheric emission but would be able to resolve the longitudinal-mean enhancements of CH_4 emission (Figure 6b). In addition, MIRI would capture both the CH_4 and C_2H_6 emission in a single measurement, which would more conclusively allow temperature or abundance variations to be deduced as the source of any observed morphology. Both VLT and JWST would allow longer-term evolution of the CH_4 emission and its morphology to be characterized. This would demonstrate whether the latitudinal banding and possible hotspots of CH_4 emission presented in this work are short-lived/episodic or longer-lived in nature.

4. Conclusions

We presented 7.90- and 12.27-μm images of Neptune measured by VLT-VISIR on September 16th 2008, which respectively sense CH_4 and C_2H_6 emission from its stratosphere. At 7.90 μm, a brightening of the longitudinal-mean CH_4 emission is observed in latitude bands centered at 24°S and 48°S. Within these brighter latitude bands are tentative detections of discrete hotspots of CH_4 emission. The 12.27-μm C_2H_6 emission is absent of any similar morphology. The mid-infrared images were compared with H-band (1.633 μm) images of Neptune, which sense clouds and haze in its upper troposphere and lower stratosphere. The bands of brighter CH_4 mid-infrared emission at approximately 25°S and 48°S are coincident with bands of bright (presumably CH_4 ice) clouds evidenced in the H-band images. We suggest the Neptunian troposphere and stratosphere are coupled in discrete regions. This could be in the form of: 1) 'overshoot' of strong, upwelling plumes and advection of CH_4 ice into the lower stratosphere, which subsequently sublimates into CH_4 gas; 2) generation of waves by plumes impinging on the tropopause, which impart their energy into the lower stratosphere and accelerate zonal winds. We favor the first process since the latter would be expected to produce smaller-scale morphology in the C_2H_6 emission, which is not observed. However, we cannot exclude temperature variations as the source of the morphology observed in CH_4 emission. Future and near-simultaneous measurements at near-infrared and mid-infrared wavelengths, including the James Webb Space Telescope, would allow these two explanations to be conclusively distinguished and for the evolution of the stratospheric features to be studied.

5. Acknowledgements

The research was carried out at the Jet Propulsion Laboratory, California Institute of Technology, under a contract with the National Aeronautics and Space Administration. The VISIR images were obtained by the ESO Telescopes at the La Silla Paranal Observatory under programme ID 081.C-0496(A). Some of the data presented herein were obtained at the W. M. Keck Observatory, which is operated as a scientific partnership among the California Institute of Technology, the University of California and the National Aeronautics and Space Administration. The Observatory was made possible by the generous financial support of the W. M. Keck Foundation. The authors wish to recognize and acknowledge the very significant cultural role and reverence that the summit of Maunakea has always had within the indigenous Hawaiian community. We are most fortunate to have the opportunity to conduct observations from this mountain. Co-author de Pater was supported by the National Science Foundation, NSF Grant AST-1615004 to UC Berkeley. Co-authors Fletcher, Roman and Rowe-Guerney were supported by a European Research Council Consolidator Grant under the European Union's Horizon 2020 research and innovation program, grant agreement number 723890, at the University of Leicester. We also thank both anonymous reviewers for their time and constructive feedback.

6. Data Availability

The VLT VISIR and Keck-NIRC2 data presented in this study are publically available at https://archive.eso.org/eso/eso_archive_main.html and https://koa.ipac.caltech.edu/cgi

respectively. Calibrated VLT images may also be requested from the authors.

References

Baines, K.H., Hammel, H.B., 1994. Clouds, hazes, and the stratospheric methane abundance in Neptune. Icarus 109, 20–39. doi:10.1006/icar.1994.1075.

Bezard, B., Romani, P.N., Conrath, B.J., Maguire, W.C., 1991. Hydrocarbons in Neptune's stratosphere from Voyager infrared observations. Journal of Geophysical Research 96, 18. doi:10.1029/91JA01930.

Bézard, B., Romani, P.N., Feuchtgruber, H., Encrenaz, T., 1999. Detection of the Methyl Radical on Neptune. The Astrophysical Journal 515, 868–872. doi:10.1086/307070.

Cohen, M., Walker, R.G., Carter, B., Hammersley, P., Kidger, M., Noguchi, K., 1999. Spectral Irradiance Calibration in the Infrared. X. A Self-Consistent Radiometric All-Sky Network of Absolutely Calibrated Stellar Spectra. The Astronomical Journal 117, 1864–1889. doi:10.1086/300813.

Conrath, B., Flasar, F.M., Hanel, R., Kunde, V., Maguire, W., Pearl, J., Pirraglia, J., Samuelson, R., Gierasch, P., Weir, A., Bezard, B., Gautier, D., Cruikshank, D., Horn, L., Springer, R., Shaffer, W., 1989. Infrared observations of the Neptunian system. Science 246, 1454–1459. doi:10.1126/science.246.4936.1454.

Conrath, B.J., Flasar, F.M., Gierasch, P.J., 1991. Thermal structure and dynamics of Neptune's atmosphere from Voyager measurements. Journal of Geophysical Research 96, 18. doi:10.1029/91JA01859.

de Pater, I., Fletcher, L.N., Luszcz-Cook, S., DeBoer, D., Butler, B., Hammel, H.B., Sitko, M.L., Orton, G., Marcus, P.S., 2014. Neptune's global circulation deduced from multi-wavelength observations. Icarus 237, 211–238. doi:10.1016/j.icarus.2014.02.030.

de Pater, I., Gibbard, S.G., Hammel, H.B., 2006. Evolution of the dusty rings of Uranus. Icarus 180, 186–200. doi:10.1016/j.icarus.2005.08.011.

Encrenaz, T., Orton, G.S., Leyrat, C., Puetter, R.C., Friedson, A.J., Pantin, E., 2007. First Thermal IR Images of Neptune: Evidence forSouthern Polar Heating and Methane Escape. The Messenger 130, 23–31.

Fletcher, L.N., Drossart, P., Burgdorf, M., Orton, G.S., Encrenaz, T., 2010. Neptune's atmospheric composition from AKARI infrared spectroscopy. Astronomy & Astrophysics 514, A17. doi:10.1051/0004-6361/200913358, arXiv:1003.5571.

Fletcher, L.N., Hesman, B.E., Achterberg, R.K., Irwin, P.G.J., Bjoraker, G., Gorius, N., Hurley, J., Sinclair, J., Orton, G.S., Legarreta, J., García-Melendo, E., Sánchez-Lavega, A., Read, P.L., Simon-Miller, A.A., Flasar, F.M., 2012. The origin and evolution of saturn's 2011-2012 stratospheric vortex. Icarus 221, 560–586. doi:10.1016/j.icarus.2012.08.024.

505 Fletcher, L.N., Hesman, B.E., Irwin, P.G.J., Baines, K.H., Momary, T.W.,
506 Sanchez-Lavega, A., Flasar, F.M., Read, P.L., Orton, G.S., Simon-Miller,
507 A., Hueso, R., Bjoraker, G.L., Mamoutkine, A., del Rio-Gaztelurrutia,
508 T., Gomez, J.M., Buratti, B., Clark, R.N., Nicholson, P.D., Sotin, C.,
509 2011. Thermal Structure and Dynamics of Saturn's Northern Springtime
510 Disturbance. Science 332, 1413. doi:10.1126/science.1204774.

511 Fletcher, L.N., Irwin, P.G.J., Orton, G.S., Teanby, N.A., Achterberg, R.K.,
512 Bjoraker, G.L., Read, P.L., Simon-Miller, A.A., Howett, C., de Kok, R.,
513 Bowles, N., Calcutt, S.B., Hesman, B., Flasar, F.M., 2008. Temperature
514 and Composition of Saturn's Polar Hot Spots and Hexagon. Science 319,
515 79. doi:10.1126/science.1149514.

516 Fletcher, L.N., Irwin, P.G.J., Sinclair, J.A., Orton, G.S., Giles, R.S., Hurley,
517 J., Gorius, N., Achterberg, R.K., Hesman, B.E., Bjoraker, G.L., 2015.
518 Seasonal evolution of Saturn's polar temperatures and composition. Icarus
519 250, 131–153. doi:10.1016/j.icarus.2014.11.022, arXiv:1412.6416.

520 Fletcher, L.N., Orton, G.S., Sinclair, J.A., Guerlet, S., Read, P., Antunano,
521 A., Achterberg, R., Flasar, F.M., Irwin, P.G.J., Bjoraker, G., Hurley, J.,
522 Hesman, B., Segura, M., Mamoutkine, A., Calcutt, S., 2018. A hexagon
523 in saturn's northern stratosphere surrounding the emerging summertime
524 polar vortex. Nature Communications 9, 3564. doi:https://doi.org/10.
525 1038/s41467-018-06017-3.

526 Fletcher, L.N., Orton, G.S., Yanamandra-Fisher, P., Fisher, B.M., Parrish,
527 P.D., Irwin, P.G.J., 2009. Retrievals of atmospheric variables on the

gas giants from ground-based mid-infrared imaging. Icarus 200, 154–175. doi:10.1016/j.icarus.2008.11.019.

Fletcher, L.N., de Pater, I., Orton, G.S., Hammel, H.B., Sitko, M.L., Irwin, P.G., 2014. Neptune at summer solstice: Zonal mean temperatures from ground-based observations, 2003–2007. Icarus 231, 146 – 167. URL: http://www.sciencedirect.com/science/article/pii/S0019103513005095, doi:https://doi.org/10.1016/j.icarus.2013.11.035.

Fouchet, T., Lellouch, E., Feuchtgruber, H., 2003. The hydrogen ortho-to-para ratio in the stratospheres of the giant planets. Icarus 161, 127–143. doi:10.1016/S0019-1035(02)00014-3.

Gibbard, S.G., de Pater, I., Roe, H.G., Martin, S., Macintosh, B.A., Max, C.E., 2003. The altitude of Neptune cloud features from high-spatial-resolution near-infrared spectra. Icarus 166, 359–374. doi:10.1016/j.icarus.2003.07.006.

Gibbard, S.G., Roe, H., de Pater, I., Macintosh, B., Gavel, D., Max, C.E., Baines, K.H., Ghez, A., 2002. High-Resolution Infrared Imaging of Neptune from the Keck Telescope. Icarus 156, 1–15. doi:10.1006/icar.2001.6766.

Gillett, F.C., Rieke, G.H., 1977. 5-20 micron observations of Uranus and Neptune. Astrophysical Journal Letters 218, L141–L144. doi:10.1086/182593.

Glasse, A.C., Atad-Ettedgui, E.I., Harris, J.W., 1997. Michelle Midinfrared Spectrometer and Imager, in: Ardeberg, A.L. (Ed.), Optical Telescopes of Today and Tomorrow, pp. 1197–1203. doi:10.1117/12.269008.

Greathouse, T.K., Richter, M., Lacy, J., Moses, J., Orton, G., Encrenaz, T., Hammel, H.B., Jaffe, D., 2011. A spatially resolved high spectral resolution study of Neptune's stratosphere. Icarus 214, 606–621. doi:10.1016/j.icarus.2011.05.028.

Hammel, H.B., Lockwood, G.W., 2007. Long-term atmospheric variability on Uranus and Neptune. Icarus 186, 291–301. doi:10.1016/j.icarus.2006.08.027.

Hammel, H.B., Lockwood, G.W., Mills, J.R., Barnet, C.D., 1995. Hubble Space Telescope Imaging of Neptune's Cloud Structure in 1994. Science 268, 1740–1742. doi:10.1126/science.268.5218.1740.

Hammel, H.B., Sitko, M.L., Lynch, D.K., Orton, G.S., Russell, R.W., Geballe, T.R., de Pater, I., 2007. Distribution of Ethane and Methane Emission on Neptune. The Astronomical Journal 134, 637–641. doi:10.1086/519382.

Irwin, P.G.J., Fletcher, L.N., Tice, D., Owen, S.J., Orton, G.S., Teanby, N.A., Davis, G.R., 2016. Time variability of Neptune's horizontal and vertical cloud structure revealed by VLT/SINFONI and Gemini/NIFS from 2009 to 2013. Icarus 271, 418–437. doi:10.1016/j.icarus.2016.01.015.

Irwin, P.G.J., Teanby, N.A., Davis, G.R., Fletcher, L.N., Orton, G.S., Tice, D., Hurley, J., Calcutt, S.B., 2011. Multispectral imaging observations of Neptune's cloud structure with Gemini-North. Icarus 216, 141–158. doi:10.1016/j.icarus.2011.08.005.

Irwin, P.G.J., Teanby, N.A., de Kok, R., Fletcher, L.N., Howett, C.J.A., Tsang, C.C.C., Wilson, C.F., Calcutt, S.B., Nixon, C.A., Parrish, P.D., 2008. The NEMESIS planetary atmosphere radiative transfer and retrieval tool. Journal of Quantitative Spectroscopy and Radiative Transfer 109, 1136–1150.

Irwin, P.G.J., Toledo, D., Braude, A.S., Bacon, R., Weilbacher, P.M., Teanby, N.A., Fletcher, L.N., Orton, G.S., 2019. Latitudinal variation in the abundance of methane (CH_4) above the clouds in Neptune's atmosphere from VLT/MUSE Narrow Field Mode Observations. Icarus 331, 69–82. doi:10.1016/j.icarus.2019.05.011, arXiv:1905.03516.

Jones, B., Puetter, R.C., 1993. Keck long-wavelength spectrometer, in: Fowler, A.M. (Ed.), Infrared Detectors and Instrumentation, pp. 610–621. doi:10.1117/12.158715.

Karkoschka, E., 2011. Neptune's cloud and haze variations 1994-2008 from 500 HST-WFPC2 images. Icarus 215, 759–773. doi:10.1016/j.icarus.2011.06.010.

Karkoschka, E., Tomasko, M.G., 2011. The haze and methane distributions on Neptune from HST-STIS spectroscopy. Icarus 211, 780–797. doi:10.1016/j.icarus.2010.08.013.

595 Lacy, J.H., Richter, M.J., Greathouse, T.K., Jaffe, D.T., Zhu, Q.,
596 2002. Texes: A sensitive high-resolution grating spectrograph for the
597 mid-infrared. Publications of the Astronomical Society of the Pacific 114,
598 153–168. doi:10.1086/338730, arXiv:arXiv:astro-ph/0110521.

599 Lagage, P.O., Pel, J.W., Authier, M., Belorgey, J., Claret, A., Doucet, C.,
600 Dubreuil, D., Durand, G., Elswijk, E., Girardot, P., Käufl, H.U., Kroes,
601 G., Lortholary, M., Lussignol, Y., Marchesi, M., Pantin, E., Peletier, R.,
602 Pirard, J.F., Pragt, J., Rio, Y., Schoenmaker, T., Siebenmorgen, R., Silber,
603 A., Smette, A., Sterzik, M., Veyssiere, C., 2004. Successful Commissioning
604 of VISIR: The Mid-Infrared VLT Instrument. The Messenger 117, 12–16.

605 Lellouch, E., Hartogh, P., Feuchtgruber, H., Vandenbussche, B., de Graauw,
606 T., Moreno, R., Jarchow, C., Cavalié, T., Orton, G., Banaszkiewicz, M.,
607 Blecka, M.I., Bockelée-Morvan, D., Crovisier, J., Encrenaz, T., Fulton, T.,
608 Küppers, M., Lara, L.M., Lis, D.C., Medvedev, A.S., Rengel, M., Sagawa,
609 H., Swinyard, B., Szutowicz, S., Bensch, F., Bergin, E., Billebaud, F.,
610 Biver, N., Blake, G.A., Blommaert, J.A.D.L., Cernicharo, J., Courtin, R.,
611 Davis, G.R., Decin, L., Encrenaz, P., Gonzalez, A., Jehin, E., Kidger,
612 M., Naylor, D., Portyankina, G., Schieder, R., Sidher, S., Thomas, N.,
613 de Val-Borro, M., Verdugo, E., Waelkens, C., Walker, H., Aarts, H.,
614 Comito, C., Kawamura, J.H., Maestrini, A., Peacocke, T., Teipen, R., Tils,
615 T., Wildeman, K., 2010. First results of Herschel-PACS observations of
616 Neptune. Astronomy & Astrophysics 518, L152. doi:10.1051/0004-6361/
617 201014600, arXiv:1006.0114.

618 Lellouch, E., Moreno, R., Orton, G.S., Feuchtgruber, H., Cavalié, T., Moses,

J.I., Hartogh, P., Jarchow, C., Sagawa, H., 2015. New constraints on the CH_4 vertical profile in Uranus and Neptune from Herschel observations. Astronomy & Astrophysics 579, A121. doi:10.1051/0004-6361/201526518.

Limaye, S.S., Sromovsky, L.A., 1991. Winds of Neptune - Voyager observations of cloud motions. Journal of Geophysical Research 96, 18. doi:10.1029/91JA01701.

Lockwood, G.W., Jerzykiewicz, M., 2006. Photometric variability of Uranus and Neptune, 1950 2004. Icarus 180, 442–452. doi:10.1016/j.icarus.2005.09.009.

Lucy, L.B., 1974. An iterative technique for the rectification of observed distributions. Astronomical Journal 79, 745. doi:10.1086/111605.

Lunine, J.I., Hunten, D.M., 1989. Abundance of condensable species at planetary cold traps - The role of moist convection. Planetary & Space Science 37, 151–166. doi:10.1016/0032-0633(89)90003-2.

Luszcz-Cook, S.H., de Kleer, K., de Pater, I., Adamkovics, M., Hammel, H.B., 2016. Retrieving Neptune's aerosol properties from Keck OSIRIS observations. I. Dark regions. Icarus 276, 52–87. doi:10.1016/j.icarus.2016.04.032, arXiv:1706.05049.

Luszcz-Cook, S.H., de Pater, I., Ádámkovics, M., Hammel, H.B., 2010. Seeing double at Neptune's south pole. Icarus 208, 938–944. doi:10.1016/j.icarus.2010.03.007, arXiv:1003.3240.

Martin, S.C., de Pater, I., Marcus, P., 2012. Neptune's zonal winds from near-IR Keck adaptive optics imaging in August 2001. Astrophysics & Space Science 337, 65–78. doi:10.1007/s10509-011-0847-y.

Max, C.E., Macintosh, B.A., Gibbard, S.G., Gavel, D.T., Roe, H.G., de Pater, I., Ghez, A.M., Acton, D.S., Lai, O., Stomski, P., Wizinowich, P.L., 2003. Cloud Structures on Neptune Observed with Keck Telescope Adaptive Optics. The Astronomical Journal 125, 364–375. doi:10.1086/344943.

Meadows, V.S., Orton, G., Line, M., Liang, M.C., Yung, Y.L., Van Cleve, J., Burgdorf, M.J., 2008. First Spitzer observations of Neptune: Detection of new hydrocarbons. Icarus 197, 585–589. doi:10.1016/j.icarus.2008.05.023.

Moses, J.I., Fletcher, L.N., Greathouse, T.K., Orton, G.S., Hue, V., 2018. Seasonal stratospheric photochemistry on uranus and neptune. Icarus 307, 124 – 145. URL: http://www.sciencedirect.com/science/article/pii/S0019103517307935, doi:https://doi.org/10.1016/j.icarus.2018.02.004.

Norwood, J., Hammel, H., Milam, S., Stansberry, J., Lunine, J., Chanover, N., Hines, D., Sonneborn, G., Tiscareno, M., Brown, M., Ferruit, P., 2016. Solar System Observations with the James Webb Space Telescope. Publications of the Astronomical Society of Pacific 128, 025004. doi:10.1088/1538-3873/128/960/025004.

Orton, G.S., Aitken, D.K., Smith, C., Roche, P.F., Caldwell, J., Snyder,

R., 1987. The spectra of Uranus and Neptune at 8-14 and 17-23 microns. Icarus 70, 1–12. doi:10.1016/0019-1035(87)90070-4.

Orton, G.S., Encrenaz, T., Leyrat, C., Puetter, R., Friedson, A.J., 2007. Evidence for methane escape and strong seasonal and dynamical perturbations of Neptune's atmospheric temperatures. Astronomy & Astrophysics 473, L5–L8. doi:10.1051/0004-6361:20078277.

Orton, G.S., Fletcher, L.N., Liu, J., Schneider, T., Yanamandra-Fisher, P.A., de Pater, I., Edwards, M., Geballe, T.R., Hammel, H.B., Fujiyoshi, T., Encrenaz, T., Pantin, E., Mousis, O., Fuse, T., 2012. Recovery and characterization of Neptune's near-polar stratospheric hot spot. Planetary & Space Science 61, 161–167. doi:10.1016/j.pss.2011.06.013.

Orton, G.S., Lacy, J.H., Achtermann, J.M., Parmar, P., Blass, W.E., 1992. Thermal spectroscopy of Neptune - The stratospheric temperature, hydrocarbon abundances, and isotopic ratios. Icarus 100, 541–555. doi:10.1016/0019-1035(92)90117-P.

Richardson, W.H., 1972. Bayesian-based iterative method of image restoration∗. Journal of the Optical Society of America 62, 55–59. URL: http://www.osapublishing.org/abstract.cfm?URI=josa-62-1-55, doi:10.1364/JOSA.62.000055.

Rieke, G.H., Wright, G.S., Böker, T., Bouwman, J., Colina, L., Glasse, A., Gordon, K.D., Greene, T.P., Güdel, M., Henning, T., Justtanont, K., Lagage, P.O., Meixner, M.E., Nørgaard-Nielsen, H.U., Ray, T.P., Ressler, M.E., van Dishoeck, E.F., Waelkens, C., 2015. The Mid-Infrared

687 Instrument for the James Webb Space Telescope, I: Introduction.
688 Publications of the Astronomical Society of the Pacific 127, 584. doi:10.
689 1086/682252, arXiv:1508.02294.

690 Roddier, F., Roddier, C., Graves, J.E., Northcott, M.J., Owen, T.,
691 1998. NOTE: Neptune's Cloud Structure and Activity: Ground-Based
692 Monitoring with Adaptive Optics. Icarus 136, 168–172. doi:10.1006/
693 icar.1998.6011.

694 Roddier, F., Roddier, C., Graves, J.E., Northcott, M.J., Owen, T.,
695 2000. Erratum: Neptune's Cloud Structure and Activity: Ground-based
696 Monitoring with Adaptive Optics, Volume 136, Number 1, pp.168-172
697 (1998). Iarus 148, 320. doi:10.1006/icar.2000.6537.

698 Sánchez-Lavega, A., del Río-Gaztelurrutia, T., Delcroix, M., Legarreta, J.J.,
699 Gómez-Forrellad, J.M., Hueso, R., García-Melendo, E., Pérez-Hoyos, S.,
700 Barrado-Navascués, D., Lillo, J., International Outer Planet Watch Team
701 IOPW-PVOL, 2012. Ground-based observations of the long-term evolution
702 and death of Saturn's 2010 Great White Spot. Icarus 220, 561–576. doi:10.
703 1016/j.icarus.2012.05.033.

704 Sánchez-Lavega, A., Pérez-Hoyos, S., Hueso, R., 2004. Clouds in planetary
705 atmospheres: A useful application of the Clausius-Clapeyron equation.
706 American Journal of Physics 72, 767–774. doi:10.1119/1.1645279.

707 Schulz, B., Encrenaz, T., Bézard, B., Romani, P.N., Lellouch, E., Atreya,
708 S.K., 1999. Detection of C_2H_4 in Neptune from ISO/PHT-S observations.
709 Astronomy & Astrophysics 350, L13–L17.

Sinclair, J.A., Irwin, P.G.J., Fletcher, L.N., Moses, J.I., Greathouse, T.K., Friedson, A.J., Hesman, B., Hurley, J., Merlet, C., 2013. Seasonal variations of temperature, acetylene and ethane in Saturn's atmosphere from 2005 to 2010, as observed by Cassini-CIRS. Icarus 225, 257–271. doi:10.1016/j.icarus.2013.03.011.

Smith, B.A., Soderblom, L.A., Banfield, D., Barnet, C., Basilevksy, A.T., Beebe, R.F., Bollinger, K., Boyce, J.M., Brahic, A., Briggs, G.A., Brown, R.H., Chyba, C., Collins, S.A., Colvin, T., Cook, A.F., Crisp, D., Croft, S.K., Cruikshank, D., Cuzzi, J.N., Danielson, G.E., Davies, M.E., de Jong, E., Dones, L., Godfrey, D., Goguen, J., Grenier, I., Haemmerle, V.R., Hammel, H., Hansen, C.J., Helfenstein, C.P., Howell, C., Hunt, G.E., Ingersoll, A.P., Johnson, T.V., Kargel, J., Kirk, R., Kuehn, D.I., Limaye, S., Masursky, H., McEwen, A., Morrison, D., Owen, T., Owen, W., Pollack, J.B., Porco, C.C., Rages, K., Rogers, P., Rudy, D., Sagan, C., Schwartz, J., Shoemaker, E.M., Showalter, M., Sicardy, B., Simonelli, D., Spencer, J., Sromovsky, L.A., Stoker, C., Strom, R.G., Suomi, V.E., Synott, S.P., Terrile, R.J., Thomas, P., Thompson, W.R., Verbiscer, A., Veverka, J., 1989. Voyager 2 at Neptune: Imaging Science Results. Science 246, 1422–1449. doi:10.1126/science.246.4936.1422.

Sromovsky, L.A., Fry, P.M., Dowling, T.E., Baines, K.H., Limaye, S.S., 2001. Neptune's Atmospheric Circulation and Cloud Morphology: Changes Revealed by 1998 HST Imaging. Icarus 150, 244–260. doi:10.1006/icar.2000.6574.

Sromovsky, L.A., Limaye, S.S., Fry, P.M., 1993. Dynamics of Neptune's

Major Cloud Features. Icarus 105, 110–141. doi:10.1006/icar.1993.1114.

Sromovsky, L.A., Limaye, S.S., Fry, P.M., 1995. Clouds and circulation on Neptune: Implications of 1991 HST observations. Icarus 118, 25–38. doi:10.1006/icar.1995.1175.

Stoker, C.R., Pollack, J.B., Rages, K., King, D.M., 1987. Vertical Structure and Convective Dynamics of Methane Clouds on Uranus, in: Bulletin of the American Astronomical Society, p. 853.

Tollefson, J., Pater, I.d., Marcus, P.S., Luszcz-Cook, S., Sromovsky, L.A., Fry, P.M., Fletcher, L.N., Wong, M.H., 2018. Vertical wind shear in Neptune's upper atmosphere explained with a modified thermal wind equation. Icarus 311, 317–339. doi:10.1016/j.icarus.2018.04.009.

Wizinowich, P., Acton, D.S., Shelton, C., Stomski, P., Gathright, J., Ho, K., Lupton, W., Tsubota, K., Lai, O., Max, C., Brase, J., An, J., Avicola, K., Olivier, S., Gavel, D., Macintosh, B., Ghez, A., Larkin, J., 2000. First Light Adaptive Optics Images from the Keck II Telescope: A New Era of High Angular Resolution Imagery. Publications of the Astronomical Society of the Pacific 112, 315–319. doi:10.1086/316543.

Wong, M.H., Tollefson, J., Hsu, A.I., de Pater, I., Simon, A.A., Hueso, R., Sánchez-Lavega, A., Sromovsky, L., Fry, P., Luszcz-Cook, S., Hammel, H., Delcroix, M., de Kleer, K., Orton, G.S., Baranec, C., 2018. A New Dark Vortex on Neptune. The Astronomical Journal 155, 117. doi:10.3847/1538-3881/aaa6d6.

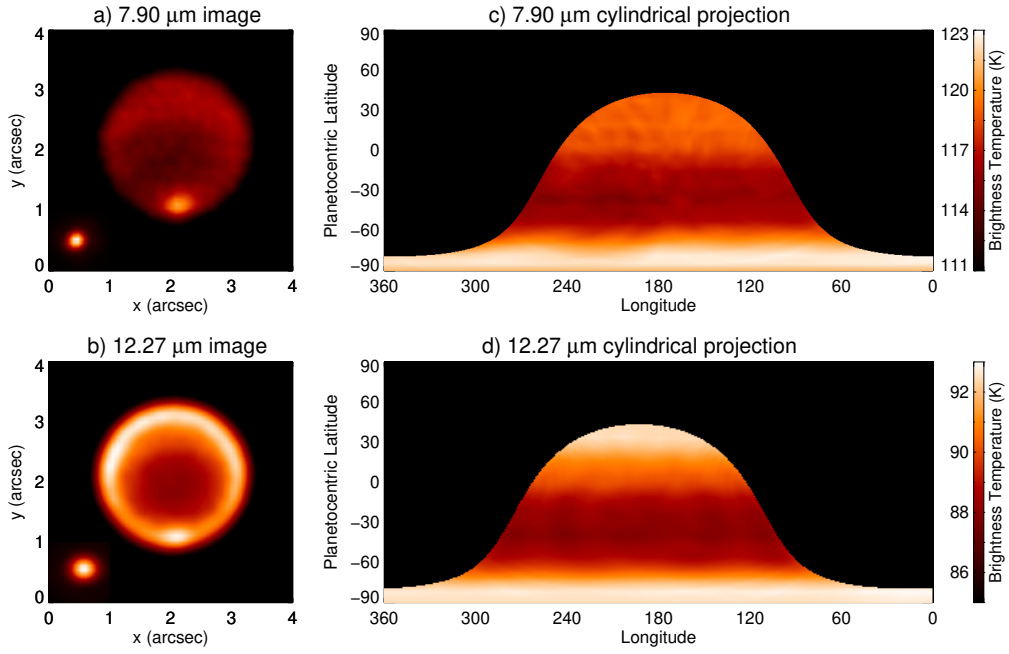

Figure 1: Panels a) and b) show coadded VLT-VISIR images of Neptune measured on September 16th 2008 at 7.90 and 12.27 µm, respectively, *before* deconvolution was performed. These images respectively capture Neptune's CH_4 and C_2H_6 emission. The corresponding images of HD 216032 are superimposed in the same panels to demonstrate the size of the point spread function. Panels c) and d) show cylindrical projections of the Neptune images in panels a) and b) following geometric fitting, radiometric calibration and a centre-to-limb correction, as described in the text.

Appendix A. Observation details

Appendix A.1. VLT-VISIR

Appendix A.2. Keck-NIRC2

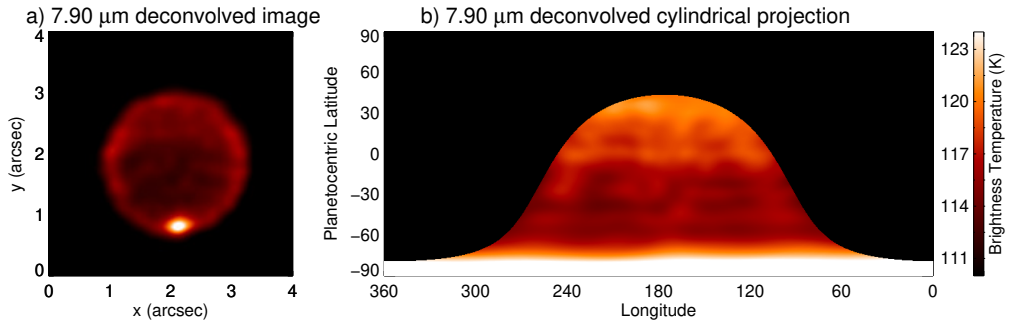

Figure 2: a) The deconvolved image of Neptune at 7.90 μm and b) the corresponding cylindrical projection.

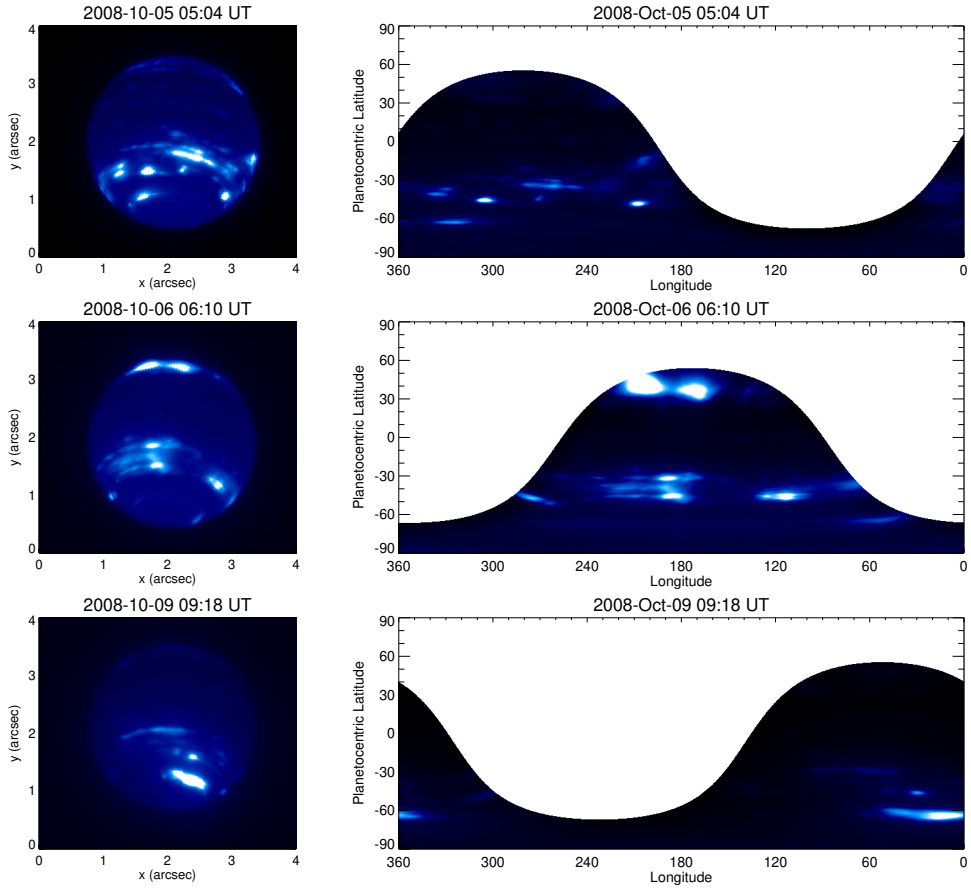

Figure 3: H-band (1.633 μm) Keck-NIRC2 images of Neptune measured between October 5 - 9th 2008 UT. The images are not radiometrically-calibrated but are proportional to the amount of reflected sunlight from clouds. The left-hand column shows the original images and the right-hand column shows cylindrical projections

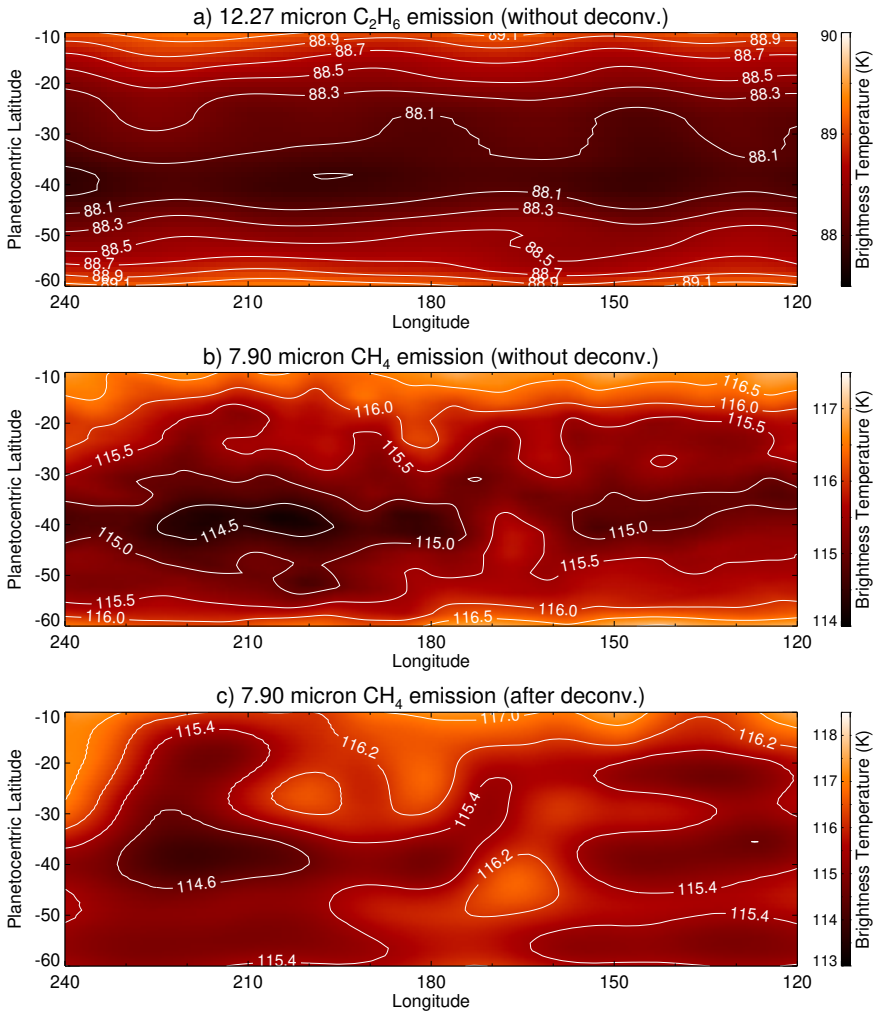

Figure 4: The images of Neptune at a) 12.27 μm and b) 7.90 μm before deconvolution and c) 7.90 μm after deconvolution. These images are also shown in Figures 1c, d and Figure 2b, but are shown again here focusing on mid-southern latitudes and with a compressed colour-scale to better highlight the smaller-scale morphology. White contours are in intervals of the noise-equivalent brightness temperatures estimated for each image, as detailed in the text.

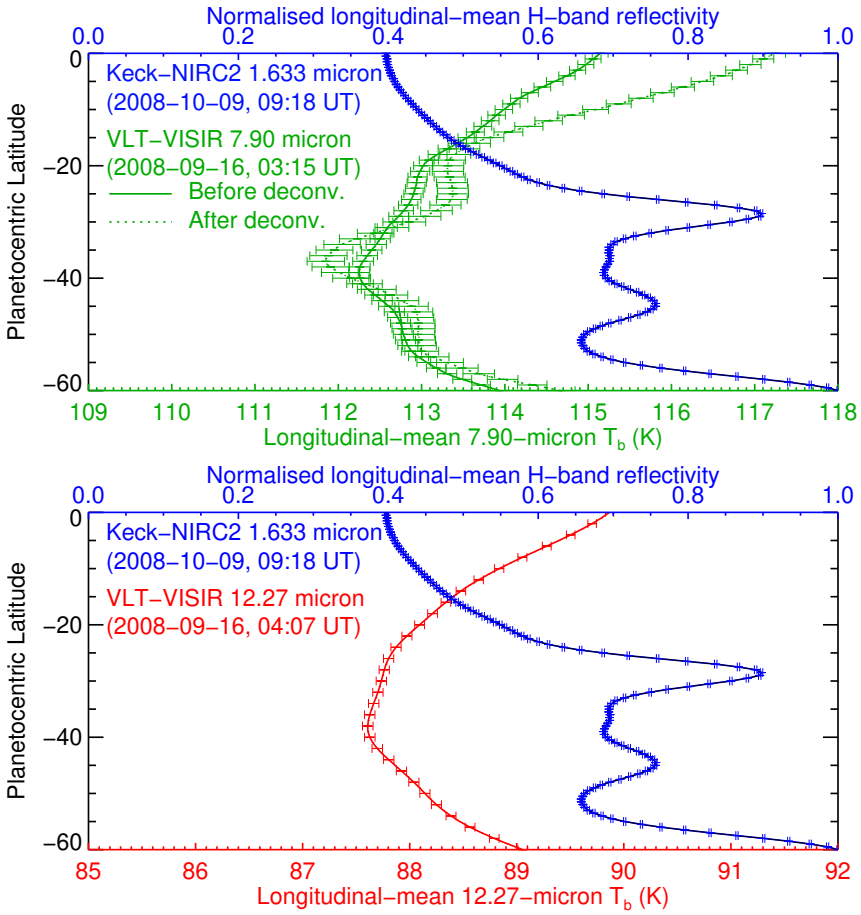

Figure 5: The longitudinal-mean brightness temperature at 7.90-μm (top panel, green) and 12.27 μm (bottom panel, red) from VLT-VISIR measurements on September 16th 2008, according to the bottom axes. For 7.90 μm, the longitudinal mean is shown for the image both before and after RCLCM deconvolution is applied, as described in the text. For comparison, the solid, blue line in both panels shows the normalized, longitudinal-mean H-band reflectivity from Keck-NIRC2 measurements on October 9th 2008, according to the top axes. The NIRC2 image was smoothed using a gaussian function such that the spatial resolutions of both sets of images were comparable. On all profiles, error bars represent the 1-σ NESR/random noise scaled by $n_{pix}^{-0.5}$, where n_{pix} is the number of pixels in each latitude circle as a measure of the data quality.

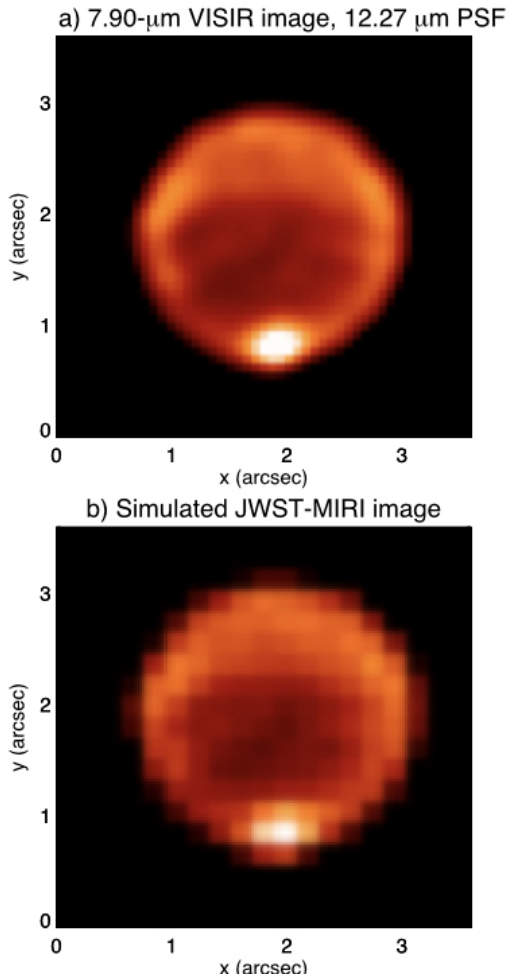

Figure 6: The deconvolved image measured by VLT-VISIR at 7.90 μm a) blurred by the PSF at 12.27 μm, b) resampled and convolved appropriate for the pixel scale and diffraction-limited spatial resolution of JWST's MIRI medium-resolution spectroscopy integral-field unit.

Object	Filter	Date	Time (UTC)	Exposure Time (s)	Airmass	Seeing (arcsec)
Neptune	J7.90	2008-Sep-16	03:01:52	345	1.021	0.75
		2008-Sep-16	03:03:56	345	1.022	0.73
		2008-Sep-16	03:05:53	345	1.023	0.73
		2008-Sep-16	03:07:40	345	1.023	0.67
		2008-Sep-16	03:09:26	345	1.024	0.70
		2008-Sep-16	03:11:23	345	1.025	0.77
		2008-Sep-16	03:13:11	345	1.027	0.67
		2008-Sep-16	03:14:60	345	1.028	0.65
		2008-Sep-16	03:16:53	345	1.029	0.66
		2008-Sep-16	03:19:01	345	1.030	0.64
		2008-Sep-16	03:20:54	345	1.032	0.70
		2008-Sep-16	03:22:48	345	1.033	0.73
		2008-Sep-16	03:24:34	345	1.035	0.81
		2008-Sep-16	03:26:27	345	1.036	0.71
		2008-Sep-16	03:28:25	345	1.038	0.67
		2008-Sep-16	03:30:12	345	1.040	0.81
		2008-Sep-16	03:32:06	345	1.042	0.73
	NeII_1	2008-Sep-16	03:45:39	362	1.057	0.97
		2008-Sep-16	04:09:57	362	1.093	0.78
		2008-Sep-16	04:19:60	362	1.113	0.78
		2008-Sep-16	04:22:20	362	1.118	0.74
		2008-Sep-16	04:24:22	362	1.122	-
		2008-Sep-16	04:26:09	362	1.126	-
		2008-Sep-16	04:27:58	362	1.130	-
		2008-Sep-16	04:29:52	362	1.134	-
HD216032	J7.90	2008-Sep-16	04:43:27	225	1.045	0.85
		2008-Sep-16	04:44:46	225	1.046	0.78
	NeII_1	2008-Sep-16	00:54:31	236	1.362	0.93
		2008-Sep-16	00:54:54	236	1.355	1.10

Table A.1: Details of the VLT-VISIR images of Neptune and HD216032. Seeing values were derived by the DIMM (Differential Image Motion Monitor) station at 0.5 μm however relative variations are valid at 7.90 and 12.27 μm. Time, airmasses and seeing represent the values at the start of each exposure. Seeing values were not available for the last four Neptune NeII_1 images.

Object	KOAID	Date (yyyy-mmm-dd)	Time (UTC)	Exposure time (s)	Airmass	Central meridian longitude
Neptune	N2.20081005.18263	2008-Oct-05	05:04:23	60.0	1.38	335.2
	N2.20081006.22213	2008-Oct-06	06:10:14	60.0	1.24	172.3
	N2.20081009.33505	2008-Oct-09	09:18:25	60.0	1.57	50.09

Table A.2: Details of the Keck-NIRC2 images of Neptune and HD 216032, including the Keck Observatory Archive Identifier (KOAID). Time and airmasses represent the values at the start of each exposure.

Appendix B. Radiative-transfer simulations

Appendix B.1. Forward model

The temperature-pressure profile and vertical profiles of gaseous species including hydrogen, helium, CH_4, C_2H_6 (the latter two being the relevant, trace gases to the wavelengths studied in this work) were adopted from Fletcher et al. (2014) and references therein. Spectroscopic line information of CH_4, C_2H_2, C_2H_6 and the collision-induced continua from H_2-H_2, H_2-He and H_2-CH_4 and CH_4-CH_4 were taken from the sources detailed in Section 2 of Fletcher et al. (2014).

Forward models were conducted using the NEMESIS software suite (Irwin et al., 2008). Forward-model radiances of Neptune were computed by performing a line-by-line calculation and convolving the resulting spectra with VISIR's 7.90-μm and 12.27-μm filter bandpasses. The vertical functional derivatives with respect to temperature were calculated for both filters and are shown in Figure B.1. The J7.90 and NeII_1 bandpasses, respectively, measure CH_4 and C_2H_6 emission predominantly from the 1-mbar level of Neptune's stratosphere. However, we note to the reader that the shape and altitudes of peak sensitivity of the contribution functions are dependent on the model atmosphere assumed.

Appendix B.2. Temperature/abundance variations

Measurements of Neptune's stratospheric emission in two discrete filter bandpasses do not provide sufficient information to invert or retrieve atmospheric information. However, we performed a series of forward-model simulations in order to

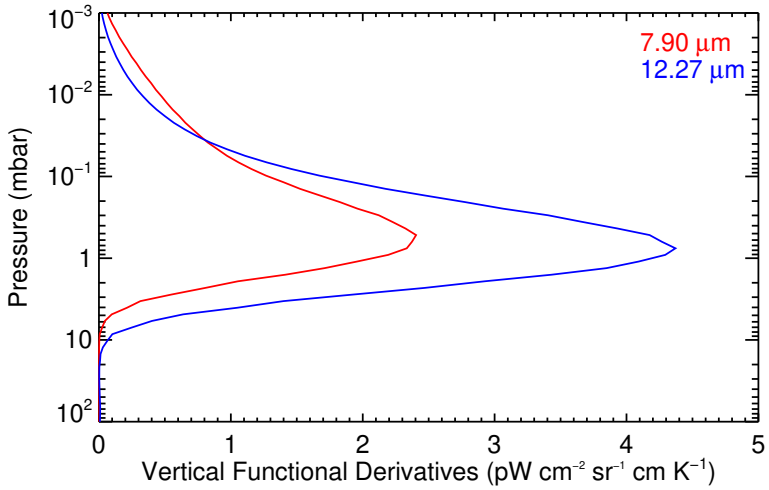

Figure B.1: The vertical functional derivatives with respect to temperature for Neptune at 7.90 µm (red) and 12.27 µm (blue). These functions describe the contribution of each atmospheric level to the total observed radiance at the top of the atmosphere.

explore what changes in the vertical profiles of temperature or CH_4 would be required to reproduce the $\Delta T_b \sim 2$ K variations in 7.90-µm CH_4 emission observed in Figure 4.

A family of vertical temperature profiles were computed by smoothly varying the profile derived by Fletcher et al. (2014) around the 1-mbar level, where the contribution function exhibits a maximum. For each temperature profile, a spectrum was forward modelled at a nadir viewing angle (to simulate the sub-observer point) and the 7.90-µm and 12.27-µm brightness temperatures were computed. These temperature profiles and the corresponding brightness temperatures are shown in Figure B.2.

Fixing the temperature profile to the black profile in Figure B.2a, a similar set of simulations and brightness temperature were computed by varying the vertical profile of CH_4 as shown in Figure B.2b. A $\sim$2-K variation in the 7.90-μm brightness temperature would require either a 5-K atmospheric temperature variation centered at the 1-mbar level or an enrichment of CH_4 at the 1-mbar level by a factor of approximately two. A 5-K atmospheric temperature variation would also produce a 1.5 - 2 K variation in brightness temperature at 12.27 μm. Variations in the CH_4 abundance have no effect on the 12.27 μm brightness temperature since the 12.27 μm filter is absent of CH_4 lines.

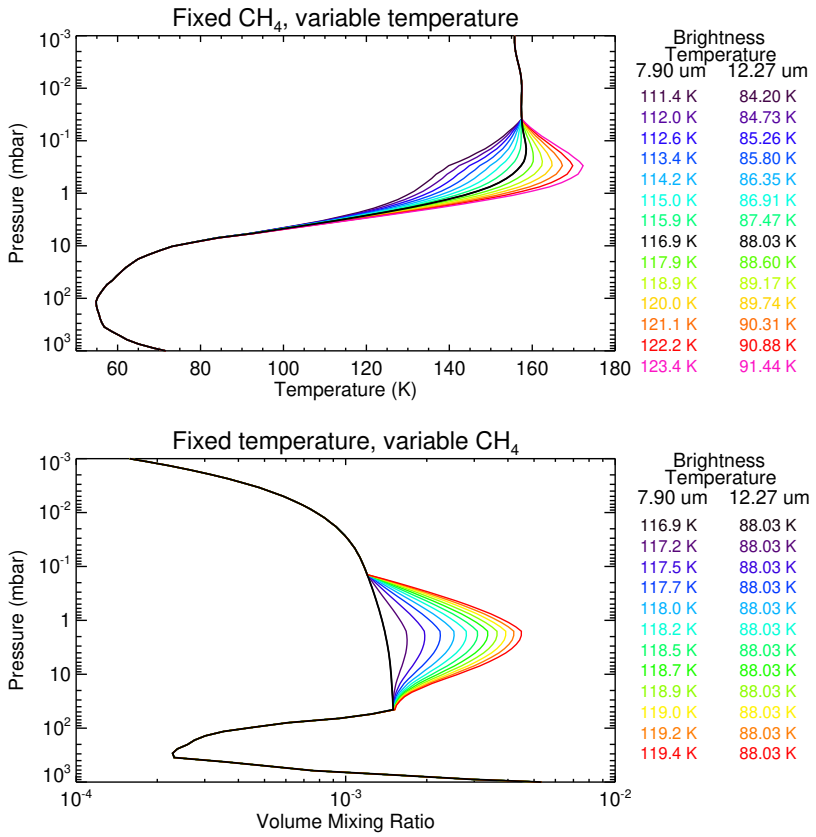

Figure B.2: Variations in the vertical profile of temperature (top panel) and CH_4 (bottom) and the corresponding forward-modelled brightness temperatures at 7.90 and 12.27 μm. The black profiles indicate the temperature and CH_4 profile adopted by Fletcher et al. (2014).